Effect of MgO–CaO–Al$_2$O$_3$–SiO$_2$ glass additive on dielectric properties of Ba$_{0.95}$Sr$_{0.05}$Zr$_{0.2}$Ti$_{0.8}$O$_3$ ceramics

Qing Xu *, Di Zhan, Duan-Ping Huang, Han-Xing Liu, Wen Chen, Feng Zhang

School of Materials Science and Engineering, Wuhan University of Technology, Wuhan 430070, People's Republic of China

ABSTRACT

MgO–CaO–Al$_2$O$_3$–SiO$_2$ glass-added Ba$_{0.95}$Sr$_{0.05}$Zr$_{0.2}$Ti$_{0.8}$O$_3$ ceramics were prepared via a wet chemical route. The effect of the glass additive on the structure and dielectric properties of the ceramics was studied. The glass additive was confirmed to be effective in promoting sintering and refining microstructure. The addition of the glass additive led to a crossover from a diffusion phase transition (DPT) to relaxor behavior. The dielectric constants of the glass-added specimens under bias electric field deviated from the behavior as predicted by the phenomenological Johnson model in a manner different from Ba$_{0.95}$Sr$_{0.05}$Zr$_{0.2}$Ti$_{0.8}$O$_3$ specimen. Furthermore, adding the glass additive resulted in a decline of energy storage capability and an enhancement of energy efficiency. These dielectric phenomena were qualitatively interpreted in relation to the polarization response of polar nano-regions (PNRs) embedded in the specimens. By balancing the energy storage capability and energy efficiency of the specimens, the preferred content of the glass additive was determined to be 5 wt.%. At an electric field of 140 kV/cm, the specimen with 5 wt.% glass additive showed an energy density of 0.42 J/cm^3 and an energy efficiency of 82.8%.

© 2013 Elsevier B.V. All rights reserved.

1. Introduction

Lead-free ferroelectric BaTiO$_3$-based solid solutions are versatile dielectrics for a variety of device applications, such as ceramic capacitors [1], piezoelectric actuators [2], electrically tunable microwave devices [3], dynamic random access memories [4] and pyroelectric detectors [5]. Recently, the application of BaTiO$_3$-based dielectric ceramics in electric energy storage has attracted growing interest by virtue of their high power density and good reliability [6–8]. It is required to improve the energy storage capability of the perovskite-type dielectrics with respect to rising demands of high power systems [9,10]. The energy storage density, U_{vol}, of polar dielectrics can be given by [7]:

$$U_{vol} = \int E dP = \int \varepsilon_0 \varepsilon(E) dE \qquad (1)$$

where E is the external electric field, P is the polarization, ε_0 is the permittivity of free space and $\varepsilon(E)$ is the dielectric constant at electric field E. It has been well recognized that a high breakdown field and a large dielectric constant at working field are preferred for achieving a high energy density. Unfortunately, BaTiO$_3$-based dielectric ceramics suffer from inevitable existence of flaws in the bulks (e.g. porosity), leading to unsatisfactory breakdown

strengths well below their intrinsic values. Meanwhile, an electric field-induced depression of polarization response renders a considerable decrease of dielectric constant for BaTiO$_3$-based ceramics under strong electric field.

In view of the energy storage applications, extensive efforts have been made on the dielectric properties of BaTiO$_3$-based ceramics. Technological and compositional strategies were employed to improve their energy storage capability. The breakdown strength of barium strontium titanate system was effectively enhanced by using a glass-ceramic strategy [9]. For BaTiO$_3$-based dielectric ceramics, liquid-phase sintering was demonstrated to be a feasible technology in promoting densification and refining microstructure. By adding glass additives, BaTiO$_3$-based dielectric ceramics gained enhanced breakdown strengths and energy densities [11–13]. On the other hand, new BaTiO$_3$-based solid solutions were developed to seek for dielectrics with desirable energy storage performance [14,15]. Composite dielectric design acts as an alternative approach to this aim. BaTiO$_3$-based dielectrics with high dielectric constants were combined with various components with high breakdown strengths, such as ferroelectric polymers and non-polar MgO [16,17]. By integrating the merits of each component, the resulting composite dielectrics obtained improved energy storage properties.

For polar dielectrics, the evolution behavior of polarization with applied electric field and attained polarization level at working field were found to be critical to the energy storage capability [10,16,18]. Therefore, the energy storage density of polar dielec-

---

* Corresponding author. Tel.: +86 27 87863277; fax: +86 27 87864580.
  E-mail address: xuqing@whut.edu.cn (Q. Xu).

trics essentially is dominated by the response of polarizable species in the materials with respect to applied electric field. Further efforts are needed to address the dielectric response of $BaTiO_3$-based dielectric ceramics under strong electric field in relation to their polarization mechanisms. A deeper insight into this issue would lead to a better understanding of the fundamental aspect of $BaTiO_3$-based dielectrics, which would in turn guide the optimization of their energy storage properties.

Producing $BaTiO_3$-based ceramics by a citrate method allows a high chemical homogeneity, an improved sinterability and a modification of dielectric properties [19]. We have prepared $Ba_{0.6}Sr_{0.4}TiO_3$ and $BaZr_{0.2}Ti_{0.8}O_3$ ceramics by the citrate method and investigated their nonlinear dielectric response under bias electric field [19,20]. In this work, we study the ferroelectric phase transition behavior, dielectric nonlinearity and energy storage properties of $MgO–CaO–Al_2O_3–SiO_2$ glass-added $Ba_{0.95}Sr_{0.05}Zr_{0.2}Ti_{0.8}O_3$ ceramics prepared via the wet chemical route. The purpose is to explore the effect of the glass addition on the dielectric properties.

2. Experimental

$Ba_{0.95}Sr_{0.05}Zr_{0.2}Ti_{0.8}O_3$ powder was synthesized by a citrate method. Reagent grade $Ba(NO_3)_2$, $Ba(NO_3)_2$, $Zr(NO_3)_4 \cdot 5H_2O$, tetrabutyl titanate and citric acid were used as starting materials. Tetrabutyl titanate was first dissolved into a citric acid solution and then various nitrates were added under stirring to form a transparent aqueous solution. The mole ratio of citric acid to the total metal cation content was 1.5. The precursor solution was heated at 300 °C to form a foam-like solid precursor. The solid precursor was pulverized and calcined at 650 °C for 1 h in air. The synthetic process was basically identical to the procedures for preparing $Ba_{0.6}Sr_{0.4}TiO_3$ and $BaZr_{0.2}Ti_{0.8}O_3$ powders [19,20].

Glass powder with the nominal composition of $5\%MgO–7\%CaO–26\%Al_2O_3–62\%SiO_2$ (weight percent) was synthesized via a similar chemical route. Reagent grade $Ca(NO_3)_2 \cdot 4H_2O$, $Mg(NO_3)_2 \cdot 6H_2O$, $Al(NO_3)_3 \cdot 9H_2O$, tetraethyl orthosilicate (TEOS) and citric acid were used as starting materials. Tetraethyl orthosilicate was dissolved into ethanol. A small amount of deionized water was added under stirring. The volume ratio of ethanol to deionized water was 6. The pH value of the solution was adjusted to around 1 by dripping acetic acid. Stirring at 60 °C yielded a transparent solution. Various nitrates and citric acid were dissolved into ethanol. A transparent solution was formed after stirring. The two solutions were mixed to form a precursor solution. The mole ratio of citric acid to the total metal cation content in the precursor solution was 2. A stirring of the precursor solution at 60 °C generated a transparent viscous gel-like precursor. The gel-like precursor was heated at 300 °C to produce a foam-like solid precursor. The solid precursor was pulverized and calcined at 600 °C for 1 h in air.

The two powders were mixed according to the nominal composition of $Ba_{0.95}Sr_{0.05}Zr_{0.2}Ti_{0.8}O_3$ + x wt.% glass (x = 0, 3, 5 and 8) and then milled with zirconia balls in distilled water. The mixed powders were uniaxially pressed under a pressure of 300 MPa into disks of 13 mm in diameter and 1 mm in thickness. Dilatometric analysis of the compacted powders was performed by a Netzsch DIL 402C dilatometer. The sintering temperature of the specimens was determined with reference to the result of the dilatometric analysis. The specimens without the glass additive (x = 0) and the glass-added specimens (x = 3, 5 and 8) were sintered at 1270 °C and 1160 °C for 2 h in air, respectively.

The morphology of the powders was observed at a Hitachi S-4700 filed emission scanning electron microscope (FESEM). X-ray diffraction (XRD) analysis of the powders and ceramic specimens were performed by a Philips X'pert PBO X-ray diffractometer using Cu Kα radiation. The microstructure of the ceramic specimens was investigated at a Jeol JSM-5610LV scanning electron microscope (SEM). Polished and thermally-etched surfaces were used for SEM investigation. The grain size of the ceramic specimens was estimated by an image analysis using the Image-Pro Plus 6.0 software. The bulk density of the ceramic specimens was measured by the Archimedes method with ethanol as medium.

The ceramic specimens were polished and painted with sliver electrode on both surfaces. The temperature dependence of the dielectric constant (ε_r) and the loss (tanδ) was measured by a TH2828 precision LCR meter (20 Hz–1 MHz) and a SSC-M10 environmental chamber (C4 controller) between −80 and 140 °C. The nonlinear dielectric properties were measured at room temperature by a TH2818 automatic component analyzer at 10 kHz under external bias electric field. A blocking circuit was adopted to protect the analyzer from applied bias voltages. Bias electric field was applied in steps of 1 kV/cm. For each applied field, dielectric data were recorded after holding at the field for 10 s. The polarization (P) vs. electric field (E) relation was measured at room temperature by a Radiant precision workstation based on the Sawyer–Tower circuit at 50 Hz. The specimens used for P–E measurement were polished to 0.5 mm in thickness.

3. Results and discussion

3.1. Structural characterization

XRD analysis of $Ba_{0.95}Sr_{0.05}Zr_{0.2}Ti_{0.8}O_3$ powder identified a single perovskite phase, while the glass powder was certified to be amorphous. These results are not shown here. Fig. 1 shows the FESEM images of the two powders. Both the powders possessed a superfine and uniform morphology, with their particle sizes being around 60 and 80 nm, respectively. The morphological features of the two powders are favorable for their homogeneous mixing.

Fig. 2 shows the XRD patterns of the ceramic specimens. The perovskite structure of the specimen with x = 0 was readily indexed in a cubic symmetry. The glass-added specimens showed a cubic perovskite structure together with small amounts of impurity phases (cordierite and anorthite) (Fig. 2a). The impurity phases are attributed to partial crystallization of the glass component during sintering. Fig. 2b illustrates the reflection of the (200) crystallographic plane of the cubic perovskite structure. No discernible change in peak shape and position could be detected, indicating that the influence of the glass additive on the cubic perovskite structure appears to be negligible.

Fig. 3 shows the SEM images of the ceramic specimens. The microstructure of the specimen with x = 0 was roughly dense (Fig. 3a). The relative density of the specimen was less than 94%. Its average grain size was estimated to be ~280 nm. The addition of the glass additive resulted in a denser microstructure with finer grains (~180 nm) (Fig. 3b–d). The relative densities of the glass-added specimens were increased to 96–97%. The effect of the glass
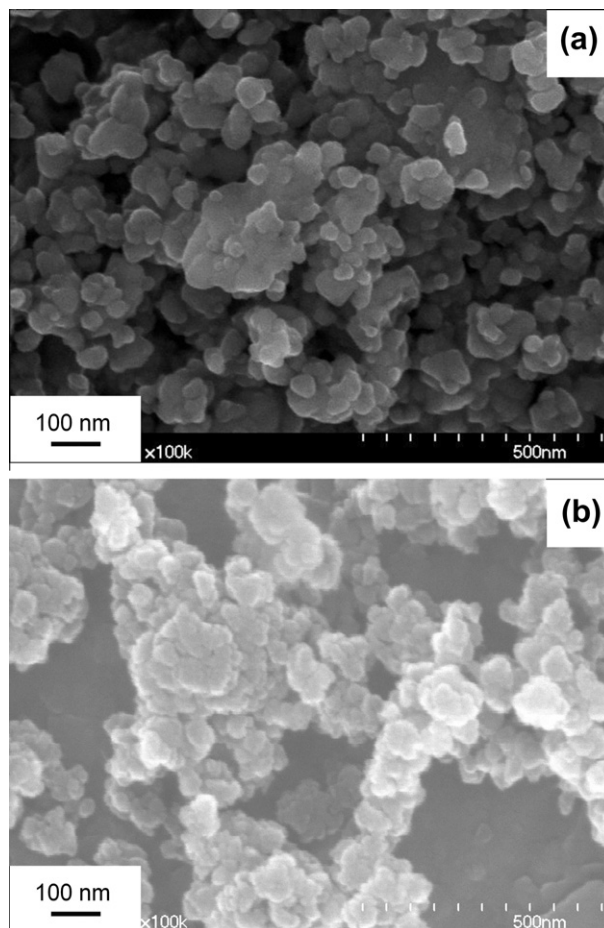

Fig. 1. FESEM images of (a) $Ba_{0.95}Sr_{0.05}Zr_{0.2}Ti_{0.8}O_3$ and (b) glass additive powders.
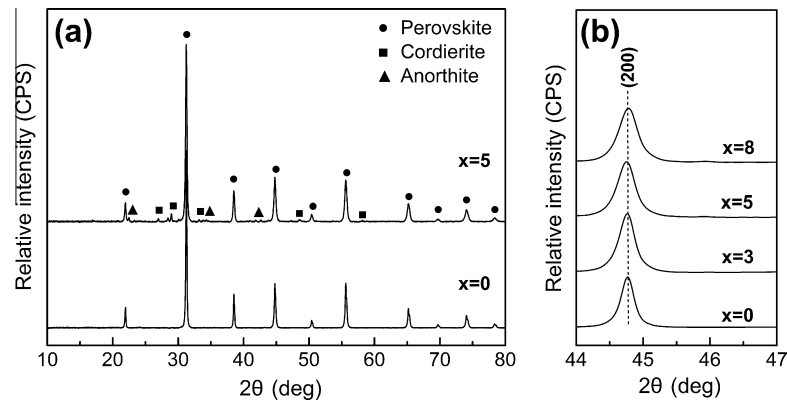
Fig. 2. XRD patterns of the specimens in the 2θ ranges of (a) 10–80° and (b) 44–47°.

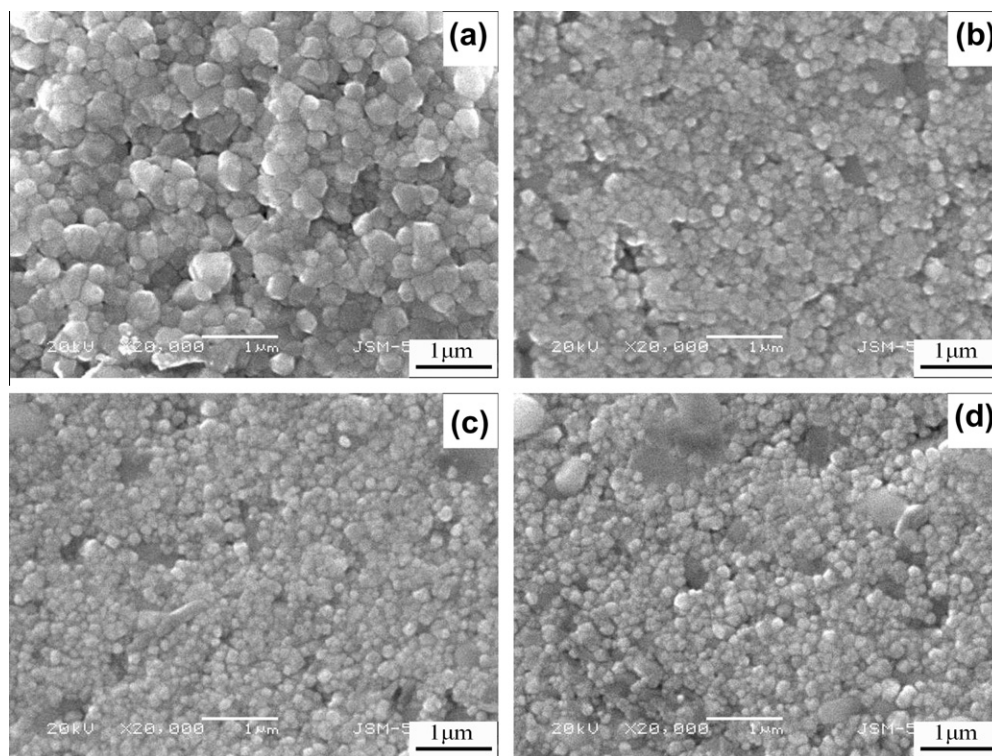**Fig. 3.** SEM images of the specimens with (a) x = 0, (b) x = 3, (c) x = 5 and (d) x = 8.

additive on microstructure is consistent with previous results [11,13]. The finer grains of the glass-added specimens can be as-cribed to a lowered sintering temperature (1160 °C) and presence of liquid phase at grain-boundaries during sintering [11].

3.2. Ferroelectric phase transition behavior

Fig. 4 shows the temperature dependence of the dielectric con-stant (ε_r) and the loss (tanδ) of the ceramic specimens at different frequencies. The specimen with x = 0 offered a diffusion phase transition (DPT) behavior, with the temperature for the maximum of the dielectric constant (T_m) being frequency-independent (Fig. 4a). The T_m value of the specimen (288 K) is lower than that of BaZr$_{0.2}$Ti$_{0.8}$O$_3$ ceramics (298 K) [20]. This result is attributable to an incorporation of Sr into the lattice. The glass-added speci-mens displayed a relaxor-like behavior (Fig. 4b–d). Moreover, the T_m values of the specimens moved to around 273 K at 10 kHz,

lower than that of the specimen with x = 0 at the same frequency. The T_m moving of the glass-added specimens is assigned to a grain size effect. The finer grains of the glass-added specimens (Fig. 3) in-creased internal stresses among the grains and thereby induced the T_m decreasing [21,22].

In order to have a closer look, the data of T_m and measurement frequency, f, of the glass-added specimens were fitted to the Vo-gel–Fulcher relation. The Vogel–Fulcher relation can be described by the following equation [23]:

$$f = f_0 \exp[-E_a/K_B(T_m - T_{VF})] \qquad (2)$$

where f_0 is the Debye frequency, E_a is the activation energy for polarization fluctuations, K_B is the Boltzmann constant, and T_{VF} is the Vogel–Fulcher freezing temperature. Fig. 5 shows the fitting plots of the specimens. For the specimen with x = 8, a very small shift of T_m with frequency disallowed performing the fitting. The plots agreed well with the Vogel–Fulcher relation, with the
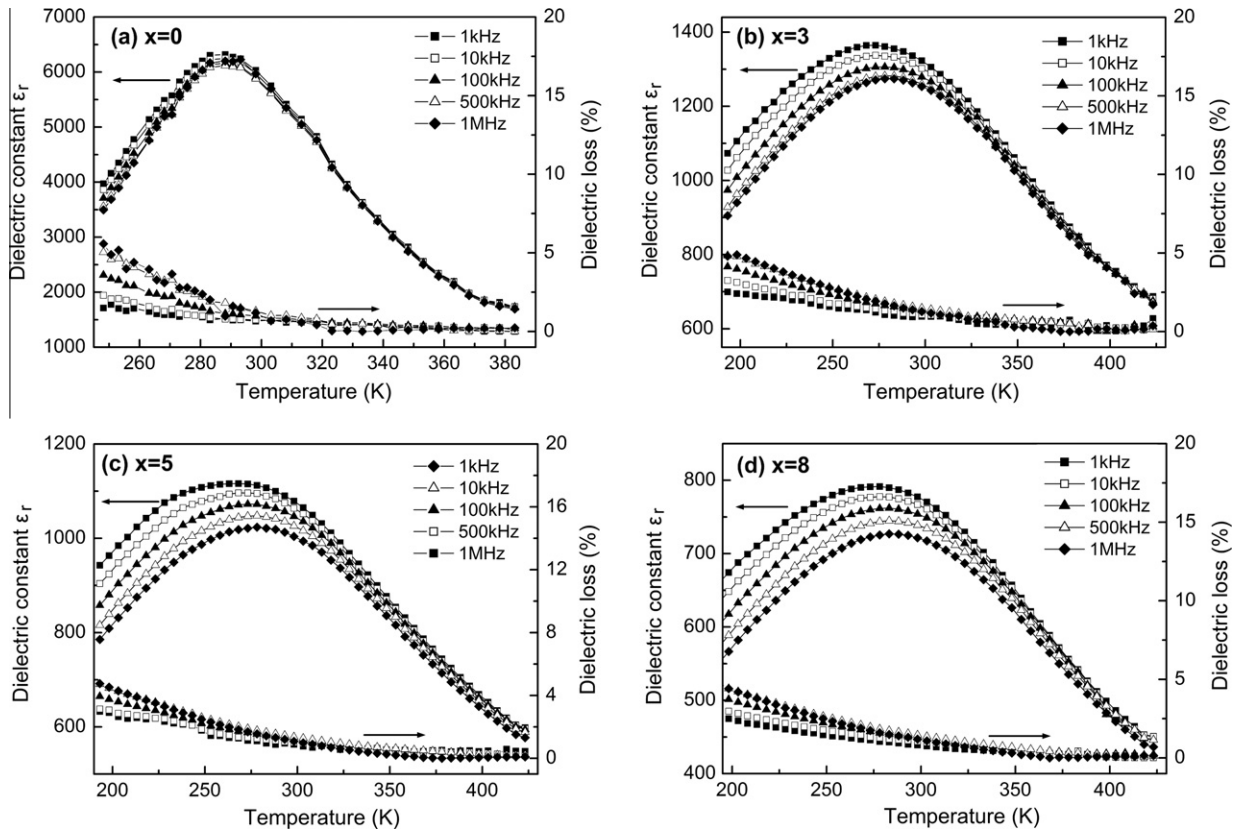
Fig. 4. Temperature dependence of the dielectric constant (ε_r) and the loss (tanδ) at different frequencies for the specimens with (a) x = 0, (b) x = 3, (c) x = 5 and (d) x = 8.
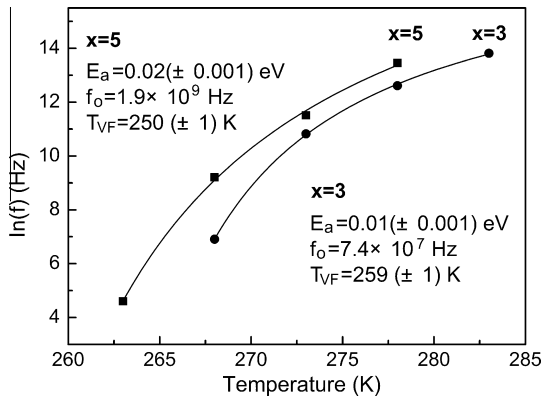

Fig. 5. Fitting plots to the Vogel–Fulcher relation for the specimens with x = 3 and x = 5, respectively.

coefficients of determination, R^2, being ~0.999. The fitting result evidences a relaxor feature of the glass-added specimens.

It has been proposed that the existence of dynamic polar nano-regions (PNRs) in a non-polar matrix is responsible for the relaxor behavior of $BaZr_xTi_{1-x}O_3$ (x = 0.25–0.75) compositions [24,25]. This picture is believed to be the case for the glass-added specimens. The E_a values of the specimens (0.01–0.02 eV), on the order of thermal energy (K_BT), coincide with thermally-activated fluctuations of local polar clusters [23]. Moreover, the E_a and f_0 data derived from the fitting are close to the results of $BaZr_{0.3}Ti_{0.7}O_3$ ceramics (E_a = 0.0156 eV and f_0 = 3.82 × 10^8 Hz) [26]. It is interesting that $BaZr_xTi_{1-x}O_3$ experiences a DPT-to-relaxor crossover within a narrow composition range from x = 0.2 to x = 0.25 [24,26]. In this sense, $BaZr_{0.2}Ti_{0.8}O_3$ appears as a threshold composition before

the emergence of a relaxor behavior. A decrease of PNR size to a critical level was regarded to be essential for the occurrence of the relaxor behavior [24]. These previous results are reminiscent of a possible cause for the crossover phenomenon of the present work, inferring a size change of PNRs with the addition of the glass additive.

3.3. Dielectric nonlinearity under bias electric field

The dielectric constants of the specimens tended to decline with increasing bias electric field in magnitude. For the specimen with x = 0 and the glass-added specimens, the tunability was calculated as the percentage of dielectric constant change at 20 and 30 kV/cm, respectively. The specimen with x = 0 showed a high tunability of 68.4%, which is analogous to the result (63.5%) of $BaZr_{0.2}Ti_{0.8}O_3$ ceramics [20]. The addition of the glass additive led to a considerable degradation of the dielectric nonlinearity. The tunabilities of the specimens with x = 3, x = 5 and x = 8 decayed to 24.6%, 22.0% and 14.6%, respectively.

The dielectric constants under bias electric field were fitted to the Johnson's phenomenological relation, as described by the following equation [27]:

$$\varepsilon_{r(E)} = \varepsilon_{r(o)}/[1 + \alpha(\varepsilon_0\varepsilon_{r(o)})^3 E^2]^{1/3} \tag{3}$$

where $\varepsilon_{r(E)}$ and $\varepsilon_{r(o)}$ represent the small-signal dielectric constants at bias field E and zero bias field, respectively, and α is the anharmonic coefficient [28]. Fig. 6 shows the fitting plots of the ceramics specimens. For each specimen, the fitting plot could be approximated by two lines. At low bias fields, the experimental data basically agreed with a linear relation, as predicted by the Johnson model. A deviation from this framework occurred at high fields. The deviation behaved in different ways, depending on the composition of the
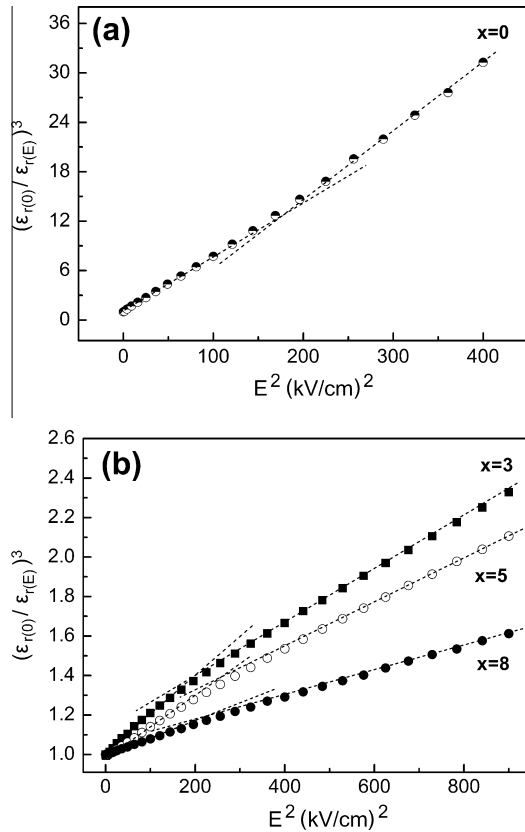
Fig. 6. $(\varepsilon_{r(0)}/\varepsilon_{r(E)})^3$ vs. E^2 plots for the specimens with (a) $x = 0$ and (b) $x = 3$, $x = 5$ and $x = 8$. The dashed lines illustrate a linear relation.

specimens. The specimen with $x = 0$ afforded a steeper line at high fields, whereas a slope reduction could be seen for the glass-added specimens. The slope reduction became less pronounced with increasing glass additive content. The deviation behavior of the specimen with $x = 0$ is identical to the result of $BaZr_{0.2}Ti_{0.8}O_3$ ceramics [20]. The slope reduction of the glass-added specimens at high fields is similar to the behavior of ZrO_2-doped $Ba_{0.55}Sr_{0.45}TiO_3$/MgO composite ceramics [29].

The Johnson relation is intended to depict the dielectric nonlinearity of polar dielectrics in the paraelectric state [27,30]. The nonlinear dielectric response of the specimens under bias electric field is essentially associated with their intrinsic polarization mechanism (i.e. lattice phonon polarization). The deviation of the fitting plots from the framework of the Johnson model implies a contribution from extrinsic mechanisms. We propose that bias field-induced polarization reorientation of PNRs is the origin of the extrinsic contribution. PNRs refer to nano-sized polar clusters made up of frozen soft phonons, which have a dynamic nature [31]. At zero bias field, the dipole moments inside PNRs thermally fluctuate between equivalent directions separated by energy barriers. Under bias electric field, the polarization of PNRs switches and aligns following the applied field. The bias field-induced polarization freeing of PNRs depresses their contribution to small-signal dielectric constant.

The relaxation time (τ) for polarization reorientation of PNRs under an external bias field can be described by the following equation [32]:

$$\tau = \tau_0 \left[\frac{U - \delta(E_{\text{int}} + E_{\text{ext}})}{K_B T} \right] \quad (4)$$

where τ_0 is a pre-exponential factor, U is the height of energy barriers between different polarization orientations, δ is a normalization coefficient, E_{int} is the internal field, E_{ext} is the applied bias

field and T is the measurement temperature. The barrier height is variable with the dimension of PNRs, with a size decrease of PNRs leading to a lower barrier height [24,25].

The different deviation behaviors of the specimens can be qualitatively understood in terms of two typical cases of PNRs. PNRs with a small size correspond to a low barrier height and thus a short relaxation time. These small PNRs are ready to flip at low bias fields, contributing to the depression of the dielectric constant. Such contribution turns faded at high bias field as the majority of PNRs have been aligned following the bias field. This is presumed to be the reason for the slope reduction of the glass-added specimens at high bias fields (Fig. 6b). On the contrary, the polarization reorientation of PNRs with a large size necessitates a longer time to reach a full relaxation. Increasing applied bias field in magnitude leads to a shortening of relaxation time, which favors the switching of these large PNRs. As a result, the reorientation of these large PNRs occurs at high bias fields, resulting in an enhanced depression of dielectric response. This circumstance is assumed to be responsible for the steeper line of the specimen with $x = 0$ at high fields (Fig. 6a).

The above discussion infers that the addition of the glass additive led to a size reduction for PNRs in the specimens. Furthermore, the decrease of the slope change in degree (Fig. 6b) suggests that the reorientation behavior of PNRs became inactive with increasing glass additive content.

Considering the extrinsic polarization of PNRs superimposed on an intrinsic paraelectric background, the dielectric constants under bias electric field were fitted to a multipolarization mechanism model as given by the following equation [30]:

$$\varepsilon_{r(E)} = \varepsilon_{r(0)}/[1 + \alpha(\varepsilon_0\varepsilon_{r(0)})^3 E^2]^{1/3} + \sum (P_0 x/\varepsilon_0) \times [\cosh(Ex)]^{-2} \quad (5)$$

where $x = P_0 V/K_B T$, and P_0 and V are the polarization and volume, respectively, on the concept of average, for extrinsic polarization entities. The first term of the equation, i.e. the Johnson term, represents the intrinsic contribution. The second term, i.e. the $\sum$ term, refers to the sum of various extrinsic contributions. In the present work, only the extrinsic contribution of PNRs was considered.

Fig. 7 shows the fitting plots to the multipolarization mechanism model for the specimens. The fitting plots is generally coinciding with the experimental data, with R^2 being 0.999, 0.993, 0.998 and 0.998 for the specimens with $x = 0$, $x = 3$, $x = 5$ and $x = 8$, respectively. The characteristic parameters of the intrinsic and extrinsic contributions to the dielectric nonlinearity were derived from the fitting. Table 1 lists the fitting results. The $\sqrt[3]{V}$ refers to the size of PNRs. The parameters of the specimen with $x = 0$ are very close to those of $BaZr_{0.2}Ti_{0.8}O_3$ ceramics, i.e., $\alpha = 4.5 \times 10^{10}$ Vm^5/C^3, $P_0 = 0.38$ (± 0.10) μC/cm^2 and $\sqrt[3]{V} = 9.1$ (± 1.0) nm [20]. With the addition of the glass additive, the anharmonic coefficient was enhanced while the polarization and size of PNRs tended to decrease. The size data of PNRs in Table 1 substantiates our inference based on the crossover phenomenon (Fig. 4) and the disparate deviation behaviors (Fig. 6).

The variation of the characteristic parameters with the addition of the glass additive can be tentatively explained in relation to an internal stress effect. As aforementioned, the refined microstructures of the glass-added specimens resulted in an increase of internal stresses among the grains. The increased internal stresses are presumed to be responsible for the larger anharmonic coefficients of the glass-added specimens [33]. Moreover, Raman study of perovskite-type ferroelectric relaxors revealed a hydrostatic pressure-induced depression of cation displacement and polar correlation length [34]. It is believed that the internal stresses among the grains behaved in the way similar to hydrostatic pressures [35]. In this context, the decrease in polarization and size of PNRs with the addition of the glass additive appears to be conceivable.
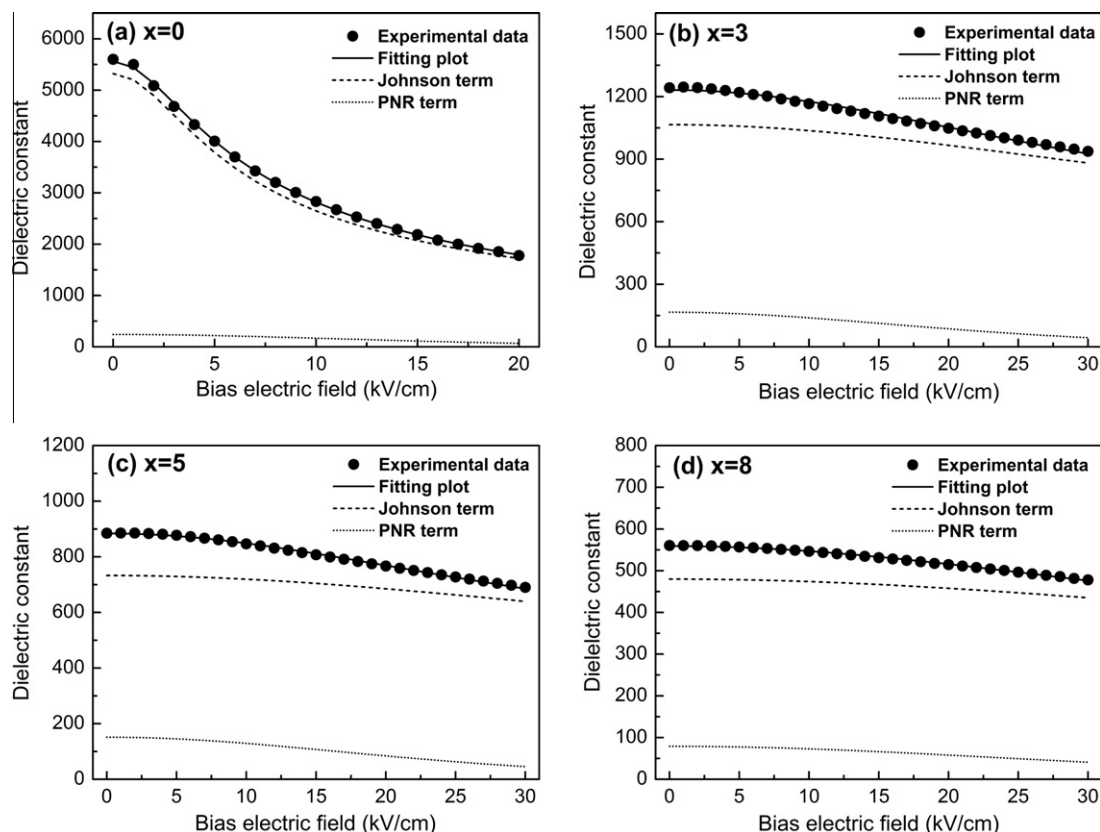
Fig. 7. Fitting plots to the multipolarization mechanism model for the specimens with (a) $x = 0$, (b) $x = 3$, (c) $x = 5$ and (d) $x = 8$.

Table 1
Characteristic parameters for various contributions to the dielectric nonlinearity of the specimens.

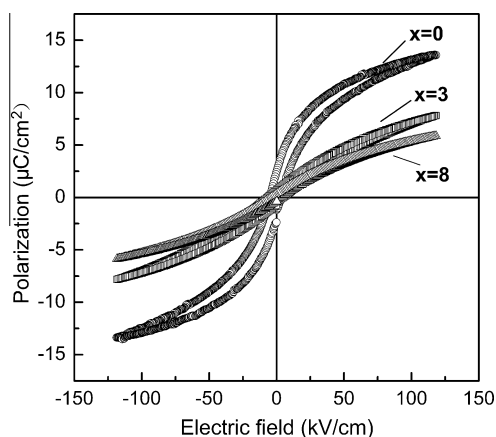| x	α (Vm^5/C^3)	P_0 (μC/cm^2)	$\sqrt[3]{V}$ (nm)
0	6.8×10^{10}	0.35 ($\pm$0.12)	9.0 ($\pm$1.3)
3	1.0×10^{11}	0.34 ($\pm$0.10)	8.0 ($\pm$1.1)
5	2.1×10^{11}	0.33 ($\pm$0.04)	7.9 ($\pm$0.50)
8	5.0×10^{11}	0.25 ($\pm$0.07)	7.8 ($\pm$1.0)

Fig. 8. P–E hysteresis loops of the specimens with different glass additive contents.

3.4. Energy storage properties

Fig. 8 shows the P–E plots of the ceramic specimens. The specimen with $x = 0$ displayed a decent hysteresis loop, giving a maximum polarization of 13.7 μC/cm^2 at 120 kV/cm. Considering the

cubic structure of the specimen (Fig. 2), the hysteresis behavior is assigned to the existence of PNRs in the macroscopically non-polar matrix of the specimen. By comparison, the glass-added specimens offered an obscure hysteresis behavior. The maximum polarizations degraded to 7.9, 7.8 and 6.0 μC/cm^2 for the specimens with $x = 3$, $x = 5$ and $x = 8$, respectively, suggesting a sluggish response of PNRs to applied electric field.

The energy storage properties were determined from the P–E loops in positive electric field region. The energy density was determined by integrating the area enclosed by the discharge curve and polarization axis in the P–E plots. The area between the charge curve and polarization axis was also calculated. The energy efficiency was achieved from the ratio of the two areas. Fig. 9 shows the energy storage properties of the ceramics specimens. The energy density of the specimen with $x = 0$ attained 0.36 J/cm^3 at 120 kV/cm, basically identical to the result of Ba$_{0.4}$Sr$_{0.6}$TiO$_3$ ceramics (0.37 J/cm^3 at 120 kV/cm) [13]. The addition of the glass additive resulted in a decline of the energy storage capability. The energy densities of the glass-added specimens tended to be lower with increasing glass additive content. On the other hand, the energy efficiencies of the glass-added specimens were obviously enhanced, showing the values in the range of 80–90% at 120–140 kV/cm. Additionally, adding the glass additive allowed an increase of applied electric field in amplitude for the specimens with $x = 5$ and $x = 8$, respectively.

From a viewpoint of microstructure, the glass-added specimens comprise more than one component different in dielectric peculiarity. Compared with the perovskite grains, the glass component and the crystallized phases at grain-boundaries, due to their non-polar nature, possess apparently lower dielectric constants. This dielectric difference resulted in a redistribution of applied electric field between the various components [36], with the field
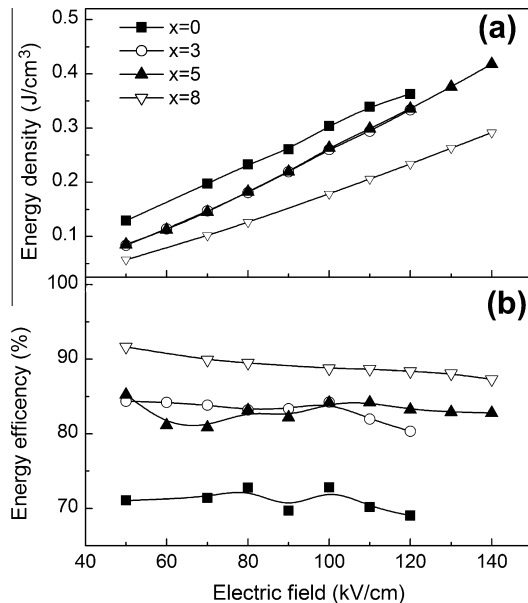
Fig. 9. Energy storage properties as a function of applied electric field for the specimens with various glass additive contents.

practically applied on the grains taking account of a minor part. This field-redistribution effect weakened the polarization response of the grains, which is responsible for the declined energy densities of the glass-added specimens. On the other hand, the field-redistribution effect is favorable to the energy efficiency. The electric field-induced orientation state of PNRs can be partially retained after removing the field [30,37]. This polarization retention behavior is believed to be the scenario to explicate the energy loss in a charge–discharge cycle. For the glass-added specimens, the depressed polarization reorientation of PNRs in the grains, correspondingly, lowered the energy loss. Consequently, the glass-added specimens achieved higher energy efficiencies as compared to the specimen with $x = 0$.

The addition of the glass additive brought about converse effects on the two parameters of the energy storage properties. The resulting change in energy storage properties is dependent on the content of the glass additive. This dependence indicates an importance of composition control in optimizing the overall properties. In the present work, the preferred content of the glass additive was determined to be 5 wt.% by balancing the two parameters. At the electric field of 140 kV/cm, the specimen with $x = 5$ achieved an energy density of 0.42 J/cm^3 and an energy efficiency of 82.8%. The energy density is roughly comparable with the result (0.44 J/cm^3) determined at about 100 kV/cm for SrO–B$_2$O$_3$–SiO$_2$ glass-added Ba$_{0.4}$Sr$_{0.6}$TiO$_3$ ceramics, while the energy efficiency is obviously higher than the previous result (67.4%) [38].

4. Conclusions

We prepared MgO–CaO–Al$_2$O$_3$–SiO$_2$ glass-added Ba$_{0.95}$Sr$_{0.05}$Zr$_{0.2}$Ti$_{0.8}$O$_3$ ceramics via a wet chemical route. The glass additive was confirmed to be effective in promoting sintering and refining microstructure. The ferroelectric phase transition behavior, dielectric nonlinearity and energy storage properties of the ceramics were studied. The results demonstrate that the dielectric properties are closely related with the polarization response of PNRs in the specimens. The evolution of the phase transition behavior and dielectric nonlinearity with the addition of the glass additive was linked to a size reduction of PNRs. Adding the glass additive

resulted in converse effects on the parameters of the energy storage properties and thus served as a viable strategy to modulate the overall properties. Based on a trade-off of the energy storage capability and energy efficiency of the specimens, the preferred content of the glass additive was determined to be 5 wt.%. At the electric field of 140 kV/cm, the specimen with 5 wt.% glass additive achieved an energy density of 0.42 J/cm^3 and an energy efficiency of 82.8%.

References

[1] D. Hennings, A. Schnell, G. Simon, J. Am. Ceram. Soc. 65 (1982) 539.
[2] P.W. Rehrig, S.E. Park, S. Trolier-McKinstry, G.L. Messing, B. Jones, T.R. Shrout, J. Appl. Phys. 86 (1999) 1657.
[3] L.C. Sengupta, S. Sengupta, Mater. Res. Innovations 2 (1999) 278.
[4] J.F. Scott, Annu. Rev. Mater. Sci. 28 (1998) 79.
[5] G.Z. Zhang, S.L. Jiang, Y.K. Zeng, Y.Y. Zhang, Q.F. Zhang, Y. Yu, J. Am. Ceram. Soc. 92 (2009) 3132.
[6] G.R. Love, J. Am. Ceram. Soc. 73 (1990) 323.
[7] N.H. Fletcher, A.D. Hilton, B.W. Ricketts, J. Phys. D: Appl. Phys. 29 (1996) 253.
[8] B.W. Ricketts, G. Triani, A.D. Hilton, J. Mater. Sci.-Mater. El. 1 (1) (2000) 513.
[9] E.P. Gorzkowski, M.J. Pan, B. Bender, C.C.M. Wu, J. Electroceram. 18 (2007) 269.
[10] B.J. Chu, X. Zhou, K.L. Ren, M.R. Lin, B. Neese, Q. Wang, F. Bauer, Q.M. Zhang, Science 313 (2006) 334.
[11] A. Young, G. Hilmas, S.C. Zhang, R.W. Schwartz, J. Am. Ceram. Soc. 90 (2007) 1504.
[12] Z.H. Wu, H.X. Liu, M.H. Cao, Z.Y. Shen, Z.H. Yao, H. Hao, D.B. Luo, J. Ceram. Soc. Jpn. 116 (2008) 345.
[13] Q.M. Zhang, L. Wang, J. Luo, Q. Tang, J. Du, J. Am. Ceram. Soc. 92 (2009) 1871.
[14] J.B. Lim, S.J. Zhang, N.C. Kim, T.R. Shrout, J. Am. Ceram. Soc. 92 (2009) 679.
[15] H. Ogihara, C.A. Randall, S. Trolier-Mckinstry, J. Am. Ceram. Soc. 92 (2009) 1719.
[16] J.J. Li, J. Claude, L.E. Norena-franco, S.I. Seok, Q. Wang, Chem. Mater. 20 (2008) 6304.
[17] Q.M. Zhang, L. Wang, J. Luo, Q. Tang, J. Du, Int. J. Appl. Ceram. Technol. 7 (2010) E124.
[18] J. Parui, S.B. Krupanidhi, Appl. Phys. Lett. 92 (2008) 192901.
[19] Q. Xu, X.F. Zhang, Y.H. Huang, W. Chen, H.X. Liu, M. Chen, B.H. Kim, J. Alloy Compd. 485 (2009) L16.
[20] Q. Xu, D. Zhan, D.P. Huang, H.X. Liu, W. Chen, F. Zhang, Mater. Res. Bull. 47 (2012) 1674.
[21] J.W. Zhai, X. Yao, X.G. Cheng, L.Y. Zhang, H. Chen, Mater. Sci. Eng. B 94 (2002) 164.
[22] X.G. Tang, J. Wang, X.X. Wang, H.L.W. Chan, Solid State Commun. 131 (2004) 163.
[23] D. Viehland, S.J. Jang, L.E. Cross, M. Wuttig, J. Appl. Phys. 68 (1990) 2916.
[24] T. Maiti, R. Guo, A.S. Bhalla, J. Appl. Phys. 100 (2006) 114109.
[25] A. Dixit, S.B. Majumder, R.S. Katiyar, A.S. Bhalla, J. Mater. Sci. 41 (2006) 87.
[26] X.G. Tang, K.H. Chew, H.L.W. Chan, Acta Mater. 52 (2004) 5177.
[27] K.M. Johnson, J. Appl. Phys. 33 (1962) 2826.
[28] J.W. Liou, B.S. Chiou, J. Am. Ceram. Soc. 80 (1997) 3093.
[29] R.H. Liang, X.L. Dong, Y. Chen, F. Cao, Y.L. Wang, Mater. Res. Bull. 41 (2006) 1295.
[30] C. Ang, Z. Yu, Phys. Rev. B 69 (2004) 174109.
[31] A.A. Bokov, M. Maglione, Z.G. Ye, J. Phys. – Condens. Matter 1 (9) (2007) 092001.
[32] M. Tyunina, J. Levoska, I. Jaakola, Phys. Rev. B 74 (2006) 104112.
[33] M. Narayanan, S. Tong, B.H. Ma, S.S. Liu, U. Balachandran, Appl. Phys. Lett. 100 (2012) 022907.
[34] J. Kreisel, P. Bouvier, B. Dkhil, B. Chaabane, A.M. Glazer, P.A. Thomas, T.R. Welberry, Ferroelectrics 302 (2004) 293.
[35] T. Badapanda, S.K. Rout, L.S. Cavalcante, J.C. Sczancoski, S. Panigrahi, E. Longo, M.S. Li, J. Phys. D: Appl. Phys. 42 (2009) 175414.
[36] K.F. Astafiev, V.O. Sherman, A.K. Tagantsev, N. Setter, J. Eur. Ceram. Soc. 23 (2003) 2381.
[37] X.F. Zhang, Q. Xu, H.X. Liu, W. Chen, M. Chen, B.H. Kim, Physica B 406 (2011) 1571.
[38] K. Chen, T.P. Pu, N. Xu, X. Luo, J. Mater. Sci. – Mater. El. 2 (3) (2012) 1599.